



**HAL**  
open science

# Combining PEDOT:PSS Polymer Coating with Metallic 3D Nanowires Electrodes to Achieve High Electrochemical Performances for Neuronal Interfacing Applications

Inès Muguet, Ali Maziz, Fabrice Mathieu, Laurent Mazonq, Guilhem Larrieu

► **To cite this version:**

Inès Muguet, Ali Maziz, Fabrice Mathieu, Laurent Mazonq, Guilhem Larrieu. Combining PEDOT:PSS Polymer Coating with Metallic 3D Nanowires Electrodes to Achieve High Electrochemical Performances for Neuronal Interfacing Applications. *Advanced Materials*, 2023, 35 (39), pp.2302472. 10.1002/adma.202302472 . hal-04234494

**HAL Id: hal-04234494**

**<https://laas.hal.science/hal-04234494>**

Submitted on 10 Oct 2023

**HAL** is a multi-disciplinary open access archive for the deposit and dissemination of scientific research documents, whether they are published or not. The documents may come from teaching and research institutions in France or abroad, or from public or private research centers.

L'archive ouverte pluridisciplinaire **HAL**, est destinée au dépôt et à la diffusion de documents scientifiques de niveau recherche, publiés ou non, émanant des établissements d'enseignement et de recherche français ou étrangers, des laboratoires publics ou privés.

# Combining PEDOT:PSS Polymer Coating with Metallic 3D Nanowires Electrodes to Achieve High Electrochemical Performances for Neuronal Interfacing Applications

Ines Muguet, Ali Maziz, Fabrice Mathieu, Laurent Mazonq, and Guilhem Larrieu\*

This study presents a novel approach to improve the performance of microelectrode arrays (MEAs) used for electrophysiological studies of neuronal networks. The integration of 3D nanowires (NWs) with MEAs increases the surface-to-volume ratio, which enables subcellular interactions and high-resolution neuronal signal recording. However, these devices suffer from high initial interface impedance and limited charge transfer capacity due to their small effective area. To overcome these limitations, the integration of conductive polymer coatings, poly(3,4-ethylenedioxythiophene)-poly(styrenesulfonate) (PEDOT:PSS) is investigated as a mean of improving the charge transfer capacity and biocompatibility of MEAs. The study combines platinum silicide-based metallic 3D nanowires electrodes with electrodeposited PEDOT:PSS coatings to deposit ultra-thin (<50 nm) layers of conductive polymer onto metallic electrodes with very high selectivity. The polymer-coated electrodes were fully characterized electrochemically and morphologically to establish a direct relationship between synthesis conditions, morphology, and conductive features. Results show that PEDOT-coated electrodes exhibit thickness-dependent improved stimulation and recording performances, offering new perspectives for neuronal interfacing with optimal cell engulfment to enable the study of neuronal activity with acute spatial and signal resolution at the sub-cellular level.


neuronal networks and neurodegenerative diseases. Indeed, capturing both action potentials and complex synaptic interactions<sup>[1]</sup> as well as performing efficient electrical stimulation demands adequate cell-electrode interfaces. For that purpose, planar Microelectrode Arrays (MEA) have been widely used to study neuronal networks both *in vivo*<sup>[2,3]</sup> and *in vitro*.<sup>[4,5]</sup> As research progresses, MEA are getting miniaturized to achieve high spatial resolution, enabling studies at several locations of a single neuron.<sup>[6]</sup> However, reducing the electrodes size decreases their effective area, which increases the electrochemical impedance, affecting the recording properties due to the combined effect of a higher thermal noise level and a lower signal amplitude due to shunt loss. This degrades the signal to noise ratio (SNR),<sup>[7,8]</sup> which results in a trade-off between device scalability and recording amplitude. As for stimulation purposes, a high impedance reduces the charge transfer at the electrode interface, which affects the possibility of injecting a safe amount of charge to the cell without causing any deleterious effect on the electrode or surrounding membrane<sup>[9]</sup> (heat accumulation, changes in local pH, gas formation, etc.).

## 1. Introduction

Recording and stimulating the electrical activity of neurons with acute spatiotemporal resolution is a fundamental step toward an in-depth understanding of the mechanisms involved in

To overcome these limitations, remarkable advances were made, thanks to the development of a new generation of MEA, in which the sensing elements are 3D-structured. Various electrode geometries have been studied at the microscale (mushroom shapes,<sup>[10–12]</sup> microneedles<sup>[13]</sup>) or at the nanoscale (nanotubes,<sup>[14,15]</sup> nanostraws,<sup>[16]</sup> or nanowires<sup>[17–22]</sup> (NWs)). These 3D structures exhibit higher effective area and spatial resolution, as well as promote tight interactions with the cells<sup>[11]</sup> that help achieve very high signal resolution compared to planar MEA, even without membrane poration.<sup>[17,22]</sup> Hence, the performances are design-dependent<sup>[14]</sup> and it is of prime importance to keep the actual optimal design (size and pitch of the nanowires), as it promotes high electrode engulfment by the cells.<sup>[23]</sup> In terms of materials, 3D-electrodes are commonly made of noble metals, such as gold (Au),<sup>[10,12,21]</sup> platinum (Pt),<sup>[19,24–27]</sup> or alloys like iridium oxide (IrOx),<sup>[15,28]</sup> titanium nitride (TiN),<sup>[29,30]</sup> platinum silicide (PtSi),<sup>[17]</sup> or indium tin oxide (ITO).<sup>[31–33]</sup> However, conventional metallic electrodes suffer from intrinsic limitations due to

I. Muguet, A. Maziz, F. Mathieu, L. Mazonq, G. Larrieu  
LAAS-CNRS  
Université de Toulouse  
CNRS  
7 avenue du colonel Roche, Toulouse F-31400, France  
E-mail: guilhem.larrieu@laas.fr

 The ORCID identification number(s) for the author(s) of this article can be found under <https://doi.org/10.1002/adma.202302472>

© 2023 The Authors. Advanced Materials published by Wiley-VCH GmbH. This is an open access article under the terms of the Creative Commons Attribution License, which permits use, distribution and reproduction in any medium, provided the original work is properly cited.

DOI: 10.1002/adma.202302472

their small effective area, high initial impedance, and low charge-transfer capacity. Moreover, the mechanical mismatch between the stiff metallic electrode and the surrounding soft neural tissue may trigger immune responses, which lead to encapsulation of the electrodes, neuronal degeneration, and subsequent device failure.<sup>[34,35]</sup>

Consequently, 3D-electrode performances must be improved through surface modification at the nanoscale to enable precise recordings and maximum charge transfer, as well as keeping the optimal designs of the electrodes, while being minimally troublesome to the tissue. Metallic and organic coatings on the electrode active site, such as IrO<sub>x</sub>,<sup>[36–39]</sup> Pt black,<sup>[40]</sup> graphene oxide,<sup>[41,42]</sup> carbon nanotubes,<sup>[43]</sup> or conductive polymers such as Poly (3,4-ethylenedioxythiophene) (PEDOT)<sup>[7,10,44–46]</sup> have been gaining considerable interest for interfacing with neurons as they can improve charge transfer and reduce the electrode impedance. PEDOT:PSS possesses well-known properties such as high conductivity, biocompatibility, and excellent stability. Last, due to its soft nature, PEDOT:PSS has the potential to reduce the mechanical mismatch at the electrode–cell interface.<sup>[34]</sup> Therefore, it is envisioned as minimally disturbing to the tissue and is an ideal candidate for improving 3D-structured electrodes performances.

Here, we combine metallic nanowire-based electrodes, made of platinum silicide (PtSi), with the remarkable properties of polystyrene sulfonate-doped PEDOT (PEDOT:PSS). We demonstrate for the first time the ability to deposit, with high selectivity, a nanoscale layer of conductive polymer coating onto the NWs using electrodeposition. The deposition was first optimized on PtSi planar microelectrodes with diameters ranging from 80 to 5 μm, for surface scaling, comparison with the literature, and investigation, as diameters under 10 μm are not commonly studied. Electrochemical depositions were then performed on PtSi NWs, and parameters were tuned to obtain nanolayers of PEDOT:PSS. All coated probes were electrochemically assessed, and PtSi electrodes were tested as controls. Electrochemical impedance measurements were used to evaluate the improvement of the recording performances, and cyclic voltammetry measurements were performed to evaluate the charge storage capacity. Voltage transient experiments were completed to investigate the electrodes behavior under electrical stimulation conditions. All coated electrodes were also morphologically characterized using scanning electron microscopy, in order to establish a direct relationship between the synthesis conditions, the layer morphology, and the electrical features.

## 2. Results and Discussion

### 2.1. PEDOT:PSS Coating Optimization on Planar Microelectrodes

For the first part of the study, we used a microfabricated MEA device composed of planar platinum-silicide microelectrodes, structured on a silicon-on-insulator substrate, with diameters ranging from 5 to 80 μm. All access lines are insulated from the liquid media; however, it is worth mentioning that part of them is exposed, which thus adds 4 μm<sup>2</sup> of conductive surface to each electrode, as shown in **Figure 1a**. This additional active area has been considered in all experiments and calculations. Details about the microfabrication can be found in the experimental section. All PEDOT:PSS electrochemical depositions were optimized on this

planar design first prior to coating nanowire-based electrodes to facilitate the implementation on 3D-nanostructures by targeting the same range of surfaces, study the effect of surface scaling, and make the positioning with literature easier.

The electrodeposition route is an important parameter, as it affects the growth of the polymer, its morphology, and its electrochemical properties. In this study, we investigated two electrochemical depositions, each performed through an oxidation process by either the application of a constant current (galvanostatic mode) or a potential scanning through cyclic voltammetry (potentiodynamic mode). Both depositions were performed in aqueous media using a conventional three-electrode cell configuration, as illustrated in **Figure 1b**, in which the microelectrodes were coated individually. The PtSi microelectrode was used as the working electrode (WE), a thick Pt wire was used as the counter electrode (CE), and a commercial Ag/AgCl electrode was used as the reference electrode (RE).

Galvanostatic (GS) deposition was carried out at a current density of 10 pA μm<sup>-2</sup> and a temperature of 21 ± 1 °C until a total charge of 1.9 nC μm<sup>-2</sup> was consumed. A relatively low synthesis potential at the initial stage of the GS synthesis (750 mV) suggests the polymerization of the adsorbed oxidized monomer layer. The GS electropolymerization process has not yet been fully elucidated; nonetheless, several mechanisms are commonly accepted.<sup>[45,47–49]</sup> In such mechanisms, the initial potential rise is caused by the evolution of the monomer concentration gradient, and is followed by a primary nucleation process divided between the induction period (monomer oxidation and oligomerization) and progressive steady nucleation, followed by 2D and 3D growths of the conductive polymer on the PtSi surface. This forms a positively charged PEDOT polymer structure, with a negatively charged PSS doping agent acting as a counter ion. In potentiodynamic deposition (PD), electrodes were cycled from –0.7 to 1 V, at a scan rate of 10 mV s<sup>-1</sup> for two cycles. The cyclic voltammogram (CV) shown in **Figure 1d** is typical of what has been reported elsewhere in PD electropolymerization conditions.<sup>[48]</sup> The oxidation current is observed at positive potentials higher than 750 mV. This feature is attributed to the oxidation of the monomer prior to polymerization through mass transport and charge transfer processes. A nucleation loop is then observed between the forward scan and reverse scan in the CV, which is associated with the initial stage of the nucleation process of the PEDOT:PSS film.

The morphologies of the PEDOT:PSS coatings obtained by both GS and PD modes have been inspected using optical and scanning electron microscopy (SEM). Both electrochemical deposition routes provide an individual, precisely localized coating onto the conductive part of the electrode, as seen in **Figure 1e**. SEM images in **Figure 1f** demonstrate that all electrode diameters, from 5 to 80 μm, were uniformly covered in PEDOT:PSS. However, the surface morphology was found to be dependent on the deposition route used for the PEDOT synthesis. The structure of PEDOT in GS conditions appears thin and smooth, with a very localized and uniform surface. This is due to the low polymerization rate and low deposition charge, which induce a controlled deposition. On the other hand, PEDOT:PSS deposited in PD conditions produced a highly porous globular 3D structure with an uncontrolled and inhomogeneous distribution. In addition, the polymer quantity deposited onto small electrodes

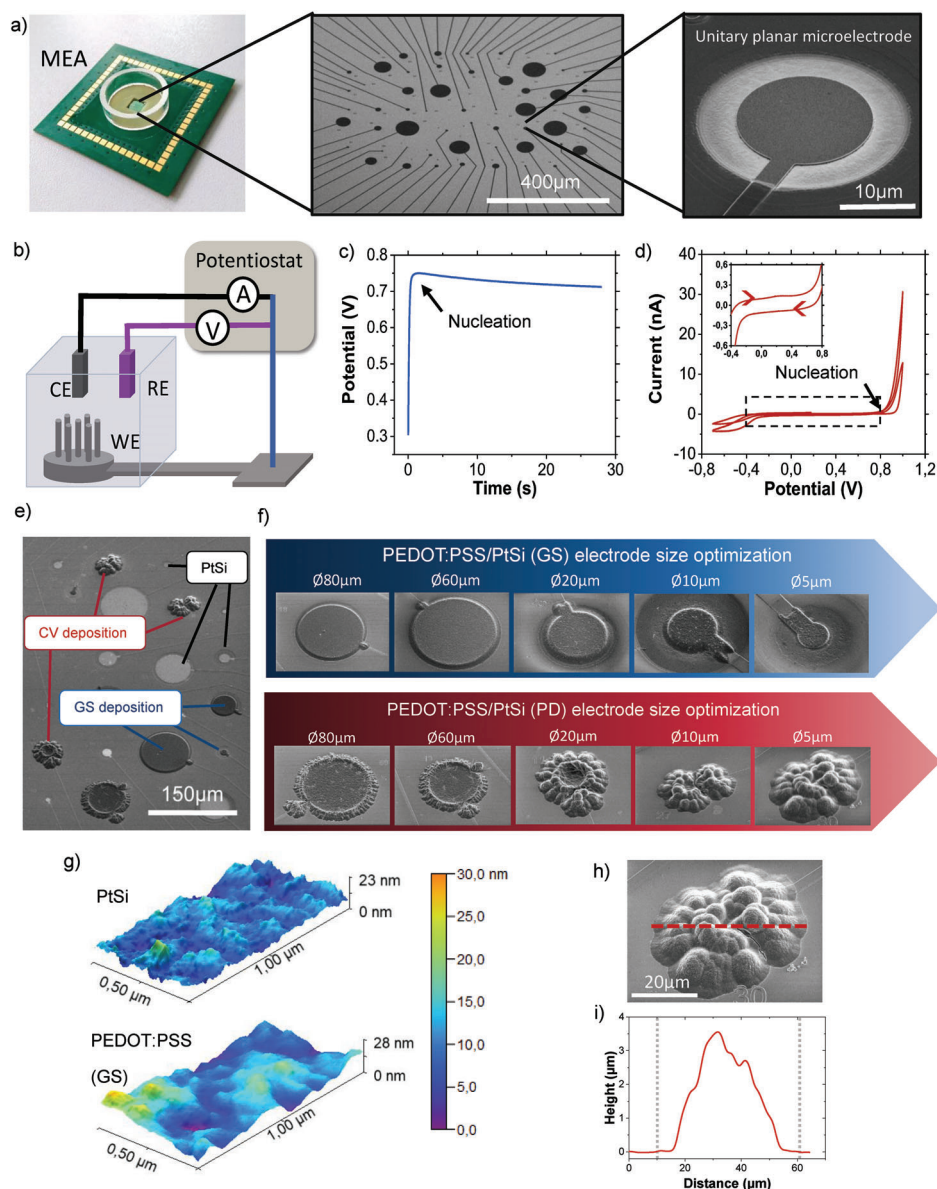


**Figure 1.** Coating optimization on planar electrodes. a) Picture of the MEA device with SEM images showing the electrodes design. b) Schematic of the conventional three electrodes system, showing the working electrode (WE), the counter electrode (CE) and the reference electrode (RE). c) Galvanostatic deposition curve represented as potential versus time. d) Graph showing the cyclic voltammetry deposition. e) SEM picture showing an electrode array in which bare, GS coated and PD-coated electrodes can be observed. This demonstrates the selectivity of the deposition. f) SEM images of GS-coated electrodes (blue) and PD-coated electrodes (red) with diameters ranging from 80 to 5  $\mu\text{m}$ . g) AFM measurements of PtSi and PEDOT:PSS (GS coated) surfaces. h) SEM image showing the scan path (red) of the profilometer on a 5  $\mu\text{m}$  PD-coated electrode. i) Profilometer trace of a 5  $\mu\text{m}$  PD-coated electrode showing the height and length of the deposition.

( $\varnothing < 20 \mu\text{m}$ ) exceeds the electrode diameter, making it difficult to evaluate the real active surface. The micron-scale surface structure of PtSi, GS-coated electrodes has been characterized and compared with Atomic Force Microscopy (AFM). Results are represented in Figure 1g, and the rugosity has been calculated (RMS Sq, 2.811 nm, 4.683 nm for PtSi and GS-coated electrodes, respectively). A slight increase in the rugosity of the surface, hence an augmentation in the active area when coated, can be observed in the case of GS-coated electrodes. The quantity of PEDOT:PSS deposited via PD 5  $\mu\text{m}$  electrodes has been estimated with a

profilometer scan, as exposed in Figure 1h,i. The PEDOT:PSS coating is  $\approx 50 \mu\text{m}$  long and 3.5  $\mu\text{m}$  high, which greatly exceeds the initial planar dimensions of the electrode and opens new perspectives for 3D-microstructurations of planar microelectrodes.

Both deposition routes present very different features, almost opposite. PD-deposited PEDOT:PSS layers tend to form 3D micro-structures, which exceptionally increase the active area of the electrode. On the other hand, the GS is more controlled, homogeneous, and precise, which likely makes it more compatible with and integrated with nanowires.

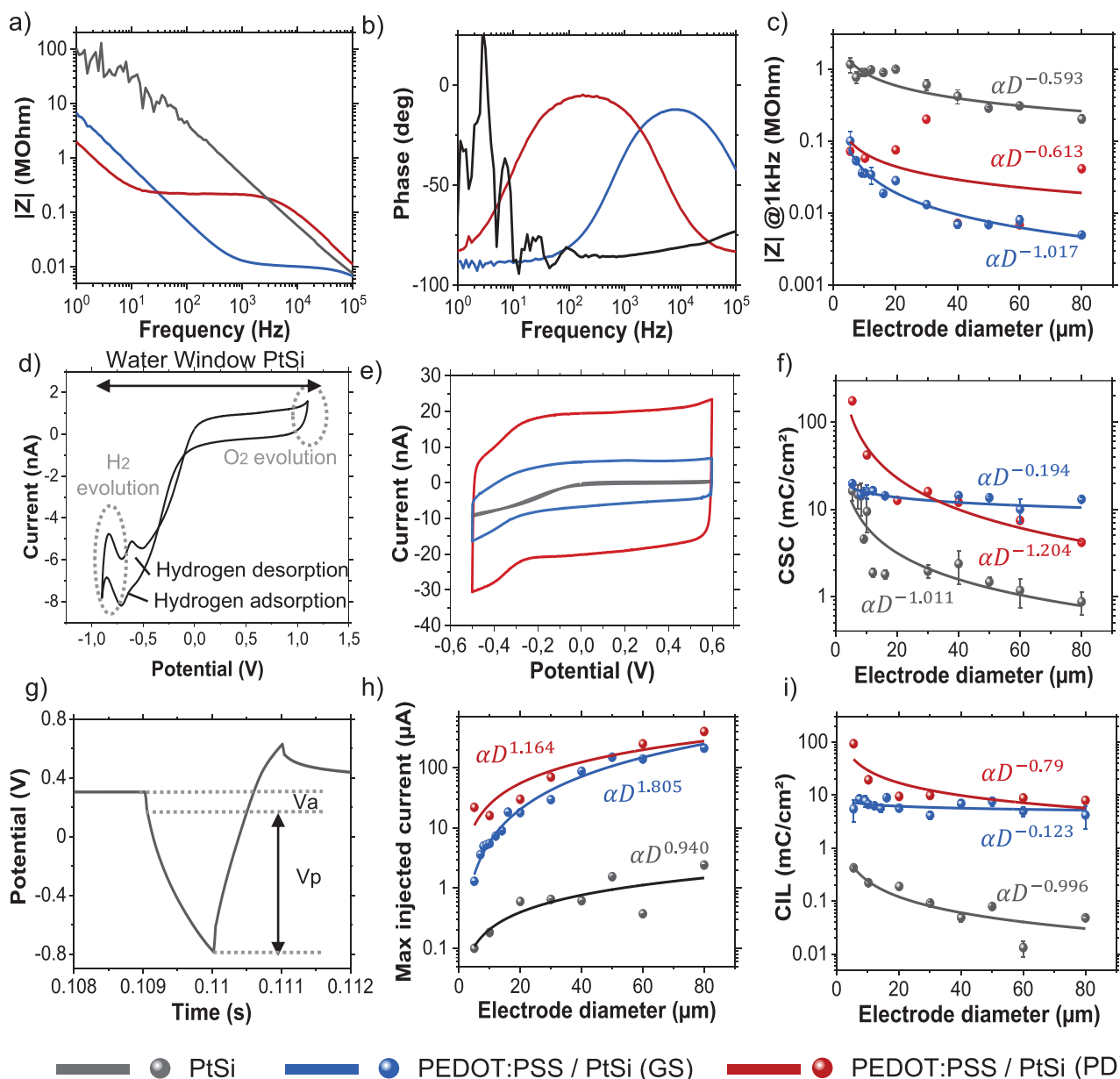


**Figure 2.** Complete electrochemical characterization of planar electrodes. a) Impedance modulus versus frequency of a bare, PD-coated, and GS-coated  $\varnothing 30 \mu$ m electrode. b) Phase versus frequency of a bare, PD-coated, and GS-coated  $\varnothing 30 \mu$ m electrode. c) Impedance modulus value at 1 kHz as a function of diameter for bare, PD-coated, and GS-coated electrodes. d) Cyclic voltammogram of an uncoated PtSi  $\varnothing 30 \mu$ m electrode. e) Cyclic voltammograms of a bare, PD-coated, and GS-coated  $\varnothing 30 \mu$ m electrode. f) Charge Storage Capacity values of bare, PD-coated, and GS-coated electrodes as a function of diameter. g) Voltage transient of a  $\varnothing 60 \mu$ m PtSi electrode at 4  $\mu$ A injection.  $V_a$  and  $V_p$  represent the access potential and the polarization potential respectively. Here,  $V_p$ , the polarization potential, equals the cathodic water window limit value, meaning it reaches the CIL. h) Current injection limit as a function of diameter for uncoated and coated electrodes. i) Charge Injection Limit as a function of diameter for uncoated and coated electrodes.

## 2.2. Recording and Stimulation Performances of Planar Microelectrodes

The effect of PEDOT:PSS coating on PtSi planar electrodes was investigated through Electrochemical Impedance Spectroscopy (EIS), Cyclic Voltammetry (CV), and Voltage transient experiments (see details in the Experimental Section). Uncoated PtSi electrodes of identical diameters were also tested as controls. EIS

was performed on coated electrodes to assess their recording performance. Data were acquired in a two-electrode configuration using a Pt electrode as the counter electrode in the frequency range  $10^0$ – $10^5$  Hz with an amplitude of 20 mV in a 0.9%w NaCl solution. **Figure 2a,b** shows the impedance modulus ( $|Z|$ ) and phase spectra of bare PtSi, GS-coated, and PD-coated  $\varnothing 30 \mu$ m electrodes. The PtSi electrode possesses a high impedance modulus, and fluctuations within the frequency range  $10^0$ – $10^2$  are due

**Table 1.** Comparison of the electrochemical performances of both our PEDOT:PSS coated planar MEA and nanowires configuration, with comparable neuronal interfacing configurations (i.e., homogeneous conductive coating layers) reported in the literature.

Material	Shape	Electrode surface area [ $\mu\text{m}^2$ ]	Specific $ Z $ @1 kHz [ $\text{M}\Omega \mu\text{m}^{-2}$ ]	CIL [ $\text{mC cm}^{-2}$ ]	Reference
<b>PLANAR MEA</b>					
Pt	Disk	7850	424	0.2	[66]
Pt	Disk	7850	1570	0.83	[46,52]
Au	Disk	7850	1570	0.2	[46,52]
PtIr	Wire	4500	405	0.13	[67]
IrOx/NPG	Disk	706	6.8	2.3	[68]
PEDOT:PSS/Au	Disk	61 575	121	2.5	[69]
PEDOT:PSS/Au	Disk	7850	170	0.9	[70]
PEDOT:PSS/Au	Disk	314	15.7	1.9	[46,52]
PEDOT:PSS/Au	Disk	314	9.42	6.2	[57]
PEDOT:ClO <sub>4</sub> /Au	Disk	177	70.8	/	[7]
PEDOT:CNT/Au	Disk	706	10.6	/	[71]
PEDOT:PSS/Pt	Disk	314	15.7	/	[72]
PEDOT:PSS/Pt	Disk	314	18.84	2.71	[46,52]
PEDOT:PSS/PtSi	Disk	318	6.36	6	This Work
<b>3D MICRO-ELECTRODES</b>					
Au	Mushroom	20	60	/	[10]
PEDOT:PSS/Au (thickness 100 nm)	Mushroom	20	8.84	/	[10]
<b>3D NANO-ELECTRODES</b>					
TiO <sub>2</sub>	Nanostraw-nanocavity	96	31	/	[16]
Au	Nanopillar	4.86	422	/	[15]
IrOx	Nanotube	5.13	29.7	/	[15]
Pt/Ti	Ultra-sharp Nanowire	0.628 * estimated	9.54	0.6	[73]
PEDOT:PSS/PtSi (thickness 300 nm)	Nanowires	23.8	7.14	1.4	This Work

to a lack of sensitivity of the equipment in low frequency range. The phase angle within the frequency range  $10^2$ – $10^5$  indicates a mixed capacitive-ohmic-like behavior, which is similar to what has been observed on Pt electrodes.<sup>[46]</sup> As expected, the presence of a PEDOT:PSS layer induces a lower mean impedance, as well as a change in the phase shape, implying an increase in the conductivity and electroactive area of the electrode. Thus, the transition from the capacitive regime to the series-resistance dominant regime happens at lower frequencies (from above  $10^5$  Hz for PtSi, to  $10^3$  and 10 Hz for GS-coated and PD-coated electrodes, respectively). The GS-deposited PEDOT:PSS shows a lower impedance in the capacitive regime of approximately an order of magnitude compared to bare PtSi. Due to its cauliflower-like shape, the PD deposited PEDOT: PSS layer not only augments the effective area but broadens the real electrode area as well. Hence, it exhibits an even lower mean impedance in the capacitive regime (almost two orders of magnitude lower than bare PtSi), and the earliest shift to the series-resistance dominant area. Figure 2c represents the impedance values at 1 kHz, the frequency of an action potential commonly used as a reference. The data have been fitted using allometric power functions. Fitted data demonstrate that PD-coating the electrodes lowers the impedance of about ten times across the entire diameter range. GS-coating, however, lowers it by ten times for small electrodes (from 1 to 0.1 M $\Omega$  for  $\varnothing$ 5  $\mu\text{m}$  electrodes), by 20 times for medium-sized electrodes ( $\varnothing$ 20  $\mu\text{m}$ )

and by 60 times for bigger electrodes, from 0.3 to 0.005 M $\Omega$  for  $\varnothing$ 80  $\mu\text{m}$ . Similar studies have been conducted on PEDOT:PSS/Pt electrodes with diameters of 2.5–20  $\mu\text{m}$ <sup>[33]</sup> resulting in impedance reductions of  $\approx$ 2.2 times for small diameters (5  $\mu\text{m}$ ). Electrodes with 20  $\mu\text{m}$  diameters and above, composed of PEDOT:PSS on Au, Pt, and nanostructured Pt, have been reported in the literature. Waafi et al. have reported an impedance reduction of 15 times for  $\varnothing$ 30  $\mu\text{m}$  PEDOT:PSS covered Pt electrodes.<sup>[50]</sup> Ganji et al. have observed a reduction of the impedance of 25 times for medium-sized electrodes ( $\varnothing$ 20  $\mu\text{m}$ ); however, they reported a reduction of only 20 times for bigger electrodes ( $\varnothing$ 80  $\mu\text{m}$ ).<sup>[46]</sup> The impedance reduction we report for all diameters, along with the calculated specific impedance (see Table 1), indicate that our PEDOT:PSS coated electrodes can be considered at the state-of-the-art when compared to the literature.

To assess the coating influence on the electrical stimulation performances of the electrodes, cyclic voltammetry and voltage transient experiments were performed, in order to determine the cathodal Charge Storage Capacity (CSC) and Charge Injection Limit (CIL). The CSC, which represents the maximum charge available that could be reversibly injected during a cathodic pulse, is defined as the time integral under the cathodic current within the cycled region.<sup>[51]</sup> The potential range used for cycling is preferably within the water electrolysis window, whose limits are defined by the water reduction potential (cathodal limit) and the

water oxidation potential (anodal limit). Outside those limits, irreversible faradaic reactions take place, which may be deleterious for the neuronal tissue or the electrode itself.<sup>[52]</sup> The cathodic CIL is a subset of the CSC, which represents the real available charge that can be reversibly injected during cathodic pulsing. The CIL is determined using voltage transient experiments, during which the maximum injected current is determined before polarizing the electrode potential beyond the cathodal water window limit. A large CSC and CIL, and therefore a large amount of injectable charge, are desirable for maximum stimulation performance.

CV measurements were conducted using the conventional three-electrode setup mentioned above. The uncoated PtSi CV curve in Figure 2d has been obtained on a Ø30 µm electrode, within the −0.9 and 1.2 V potential range, at a scan rate of 200 mV s<sup>−1</sup> in a 0.9%w NaCl solution. The water electrolysis window of the PtSi is considered to be −0.9/1.1 V, which is similar to the typical Pt water window when cycled in PBS.<sup>[53]</sup> The typical hydrogen adsorption and desorption peaks appear between −0.5 and −0.8 V. Nonetheless, it is interesting to notice the absence of a surface oxidation area and oxide reduction peak when compared to the conventional Pt CV shape.<sup>[53]</sup> Figure 2e illustrates the CV curve of PtSi, PEDOT:PSS/PtSi (GS coated), and PEDOT:PSS/PtSi (PD-coated) Ø30 µm electrodes characterized between −0.5 and 0.6 V at 200 mV s<sup>−1</sup> to avoid any undesirable faradaic reactions. Indeed, organic electrodes usually exhibit a smaller water electrolysis window, from −0.9 to 0.6 V in the case of PEDOT:PSS/Pt or PEDOT:PSS/Au.<sup>[52]</sup> As expected, a great increase in the electroactive area can be observed. In accordance with the coating morphology, PD-coated electrodes feature a larger effective area than GS-coated probes. Additionally, the symmetry of the PEDOT:PSS/PtSi cyclic voltammograms implies that the doping process is highly reversible, which indicates promising properties regarding the ionic to electronic charge transfer at the electrode interface.<sup>[43]</sup> The cathodic CSC values of the probes has been extracted from these data, considering the initial planar area of the electrode, and results, which have been fitted using allometric power functions, and are displayed in Figure 2f. As anticipated, the CSC of the PEDOT:PSS coated electrodes is significantly higher than bare electrodes. PD-coating the electrodes increases the CSC up to 10 times for small electrodes, with 176 mC cm<sup>−2</sup> for Ø5 µm PD-coated electrodes compared to 16.3 mC cm<sup>−2</sup> for Ø5 µm PtSi electrodes. The CSC is increased up to five times for larger electrodes, with 4.16 mC cm<sup>−2</sup> for Ø80 µm compared to 0.25 mC cm<sup>−2</sup> for Ø80 µm PtSi electrodes. GS-coated electrodes demonstrate a distinct behavior when compared to PD-coated electrodes. They exhibit a slight increase in CSC for small electrodes (Ø5 µm), reaching 19.7 mC cm<sup>−2</sup>, while for larger electrodes (Ø80 µm), the increase is magnified up to 52 times, resulting in a CSC of 13.03 mC cm<sup>−2</sup>. We demonstrated a very prominent improvement for small PD-coated electrodes; nonetheless, the morphology of the coating is extremely rough, and the coating exceeds the initial planar electrode active area. The improvement appears less significant in the case of small GS-coated electrodes <Ø20 µm due to the thin morphology of the coating. Nonetheless, it is important to note that the CSC can only be regarded as a relative value, as it relies on the electrode material, shape, electrolyte composition, and experiment conditions (potential range and scan rate). In addition, when cycled,

the electrode is subjected to a slow voltage ramp, which contrasts with the usual neuronal stimulation conditions.

Consequently, voltage transient experiments are more likely to represent the true electrode behavior during cell stimulation, as the probe is exposed to multiple cathodal-first, biphasic current pulses. Here, we applied symmetric cathodal-first biphasic pulses of a millisecond, with an interphase gap of 10 µs, and an interpulse delay of 95 ms.<sup>[52,54–56]</sup> An example of the voltage transient response to injected current of a Ø60 µm PtSi electrode is displayed in Figure 2g. Two slopes can be observed. The first voltage drop corresponds to the access potential ( $V_a$ ), associated with the ohmic resistance of the liquid media. The second slope, which indicates a gradual polarization at the electrode interface, is designated as the polarization potential ( $V_p$ ). Interestingly, the PtSi voltage transient is similar to the usual Pt response.<sup>[26,52]</sup> The maximum injectable current determined to calculate the CIL is considered to be when  $\Delta V_p$  reached the cathodic water window limit value<sup>[52]</sup> and is plotted in Figure 2h. Coated probes reach their limit at higher current (examples of voltage transient response for PEDOT:PSS-coated probes are displayed in Section S2, Supporting Information), meaning more charge can be injected before creating undesirable faradic reactions that are deleterious for the cell membrane or electrode itself. The corresponding CIL values have been calculated, and the results are exposed in Figure 2i. The CIL of PtSi electrodes ranges between 0.5 and 0.03 mC cm<sup>−2</sup>, and analogous results have been reported on Pt microelectrodes<sup>[52]</sup> (CIL 0.83 mC cm<sup>−2</sup>). The CIL of GS-coated probes ranges between 8 and 5 mC cm<sup>−2</sup> and PD-coated electrodes exhibit a CIL ranging from 50 to 5 mC cm<sup>−2</sup> for Ø5–Ø80 µm, respectively. Optimized PEDOT-based coatings have been reported in a similar range between 1.2 and 8.4 mC cm<sup>−2</sup>.<sup>[52,57]</sup> Yet, in the case of small electrodes (Ø5 µm), a GS-coating increases the CIL by 16 times, and this increase is greater than what has been observed on PEDOT:PSS-coated Pt electrodes of similar diameters.<sup>[52]</sup> The improvement is even greater with PD-coated results. Indeed, PD-coating increases the CIL of small electrodes by 100 times, which is particularly boosted by the cauliflower-like morphology.

The improvement of the performances induced by PEDOT:PSS coating is highly beneficial for sub 10 µm diameter electrodes, which were until now difficult to implement in MEA devices, due to the strong degradation of the global performance (impedance, SNR, current injection...) linked to the miniaturization of the surface. This opens new perspectives for electrophysiology studies with high resolution.

### 2.3. PEDOT:PSS Coating Optimization on 3D-Nanostructured Microelectrodes

For the second part of the study, we used a microfabricated device called a Nanostructured Electrode Array (NEA),<sup>[17]</sup> as shown in Figure 3a, where the sensing part is composed of seven interconnected vertical core-shell type PtSi nanowires of 3.5 µm height and 350 nm diameter each. However, the base of each nanowire remains insulated and only the upper part is exposed (further details can be found in Section S1 and Figure S2, Supporting Information), hence the recording site is 3 µm high, as

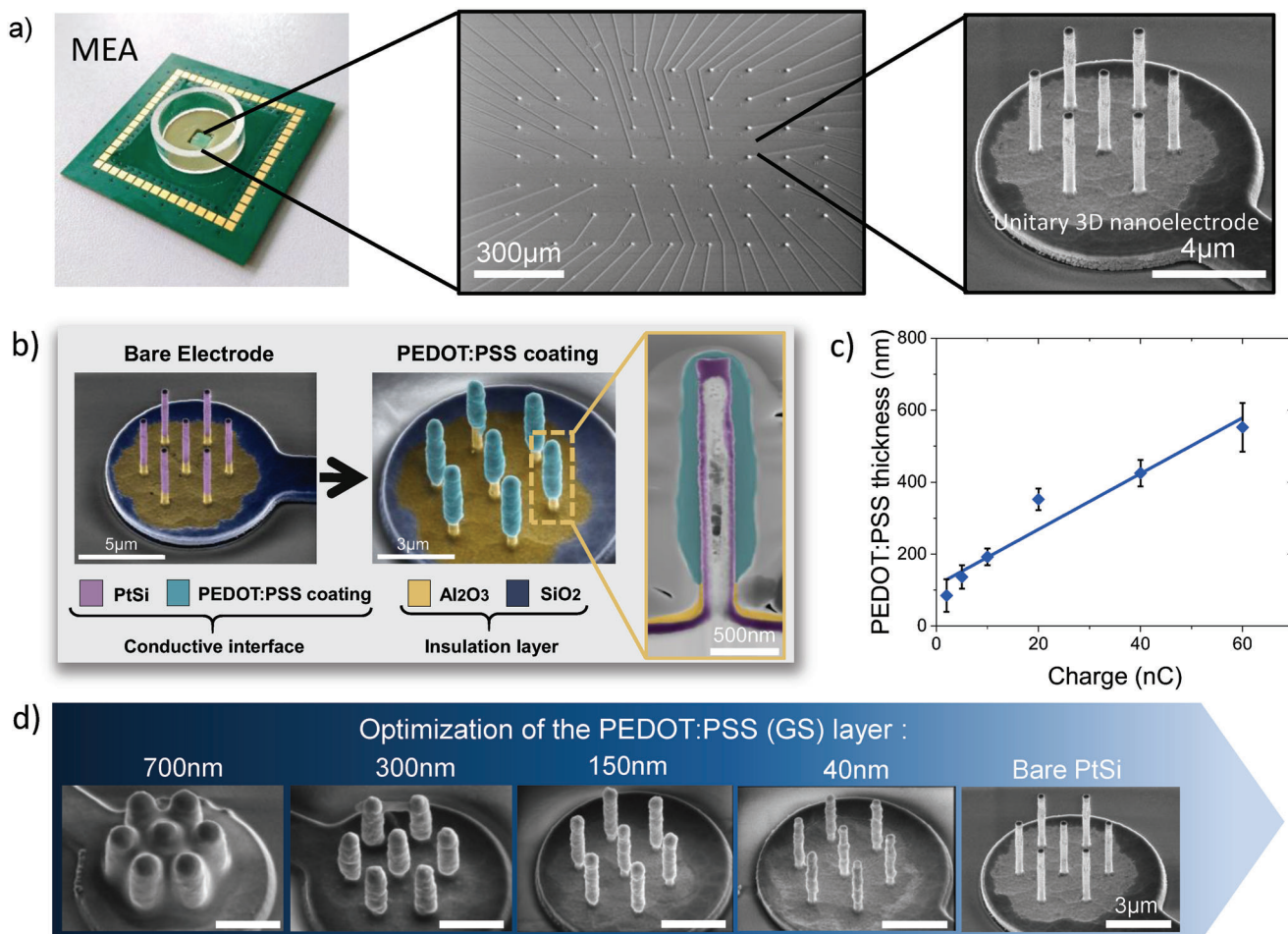


**Figure 3.** Coating thickness optimization of NWs-based electrodes. a) Picture of the NEA device with SEM images showing the electrodes design. b) SEM images of a 200 nm PEDOT:PSS coating with a high-angle annular dark-field imaging STEM-HAADF image showing the cross section of a coated nanowire. c) Graph showing the obtained PEDOT:PSS layer thickness as a function of the applied deposition charge per electrode. d) SEM images showing the coating optimization, with thicknesses varying from 700 to 40 nm.

seen on Figure 3b. The total conductive surface per electrode is estimated to be  $23.8 \mu\text{m}^2$ . Details about the fabrication process can be found in the Experimental Section. The key aspect ratio of the probes contributes to achieving a high interaction with cells<sup>[18,19,23,58,59]</sup> and thus reaching high signal resolution, therefore it has to be maintained. For that matter, nanoprobe were coated using only galvanostatic deposition to obtain a thin and conformal coating. Indeed, as expected, the PD-route leads to a rough morphology of the layer, which is incompatible with an integration on nanostructures, as illustrated in Section S1 (Figure S1, Supporting Information). Electrochemical deposition was performed in the same three-electrodes configuration as detailed above (Figure 1b), in the same electrolyte solution of 10 mM EDOT and 10 mM Na:PSS. The conductive part of the probes was successfully coated, as presented in Figure 3b. The scanning transmission electron microscopy with high-angle annular dark-field image (STEM-HAADF) showing the cross-section confirms that the PEDOT:PSS layer is dense, homogeneous, and wraps around the nanostructure tightly. Energy Dispersive X-Ray Analysis (EDX) has been performed on the coated NWs and results can be found in Section S1, Figure S2 (Supporting Infor-

mation). The conductive polymer thickness has been tuned by applying currents between 10 and 5 pA  $\mu\text{m}^{-2}$  and total consumed charges between 60 and 2 nC per electrode, which corresponds to charges varying between 2.52 and 0.084 nC  $\mu\text{m}^{-2}$  (Figure 3c). As a result, PEDOT:PSS coatings with a thickness range between 700 and 40 nm have been obtained, as represented in Figure 3d. Thin coatings were successfully achieved, meaning the preservation of the key aspect ratio of the NWs, which would imply optimal cell engulfment. Thin PEDOT:PSS depositions (the reported layer thickness is 100 nm) on 1  $\mu\text{m}$  high mushroom-shaped microelectrodes have been reported<sup>[10]</sup> as well; however, to the best of our knowledge, layers thinner than 100 nm have not yet been demonstrated.

#### 2.4. Electrochemical Impedance Spectroscopy

Similarly, to what has been done with planar electrodes, the influence of PEDOT:PSS coatings on PtSi nanowires has been measured through EIS, CV and Voltage transient experiments (see Experimental Section), and uncoated PtSi electrodes were tested



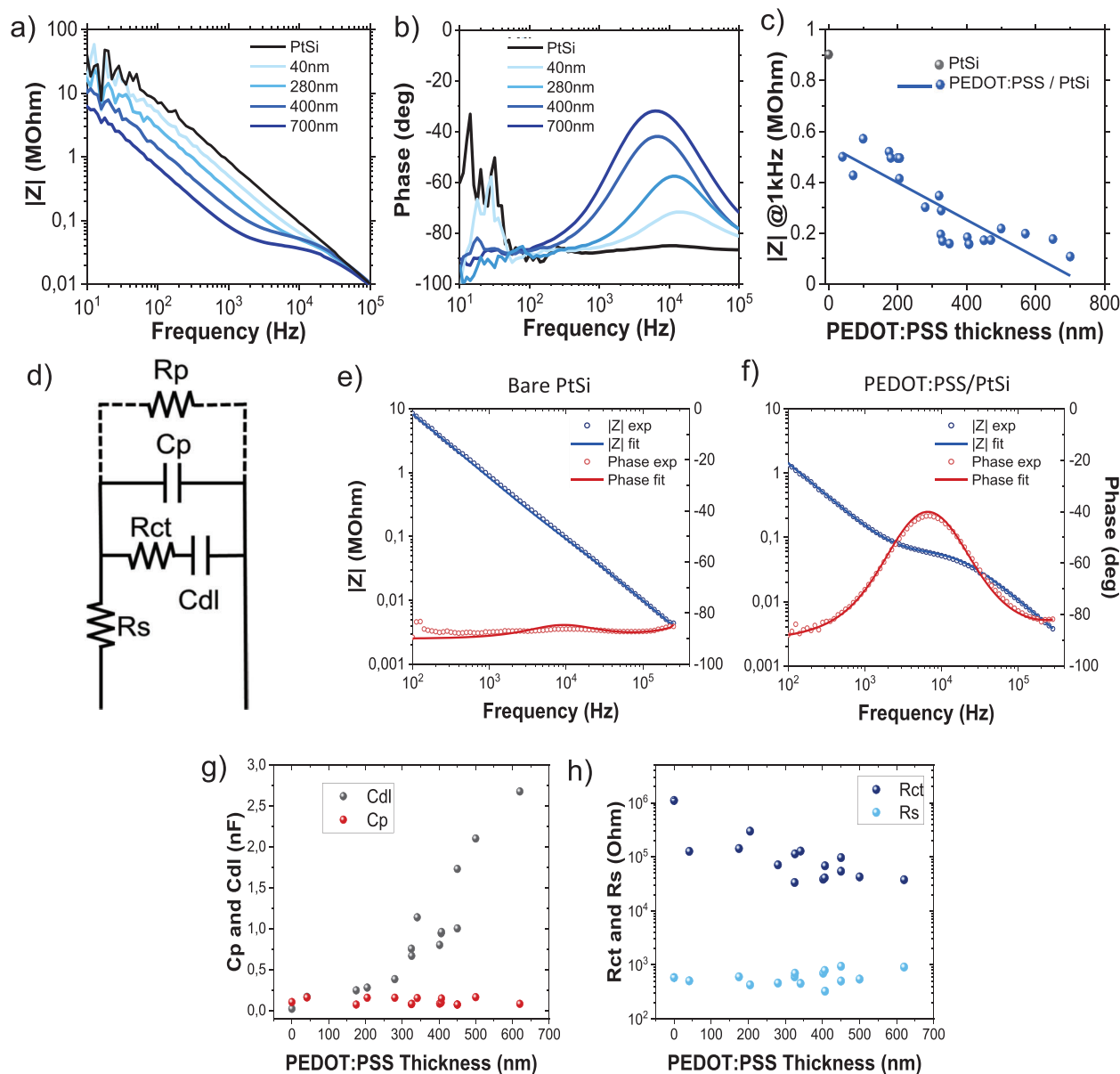


**Figure 4.** Complete electrochemical impedance characterization of NWs-based electrodes a) Impedance modulus versus frequency of bare and PEDOT:PSS coated NWs. b) Phase versus frequency bare and PEDOT:PSS coated NWs. c) Impedance modulus value at 1 kHz as a function of PEDOT:PSS coating thickness. d) Equivalent circuit model for bare PtSi electrodes and PEDOT:PSS coated electrodes using a simple 5-elements circuit, composed of an electrolyte resistance ( $R_s$ ), a charge-transfer resistance ( $R_{ct}$ ), a double layer capacitance ( $C_{dl}$ ), as well as a system capacitance ( $C_p$ ) and system resistance ( $R_p$ ). e) Graph representing the experimental and modeled impedance modulus and phase of a PtSi NWs electrode. f) Graph representing the experimental and modeled impedance modulus and phase of a coated NWs electrode (410 nm thick). g) Graph exposing the variation of  $C_{dl}$  and  $C_p$  with respect to the coating thickness. h) Graph exposing the variation of  $R_{ct}$  and  $R_s$  with respect to the coating thickness. In all the panel, the diameter of PtSi NWs is 350 nm.

as controls. As previously explained, EIS data were acquired in a two-electrode configuration using a Pt electrode as the counter electrode in the frequency range 1–10<sup>6</sup> Hz with an amplitude of 20 mV in a 0.9%w NaCl solution. The measured impedance modulus and phase spectra for bare PtSi and coated NWs, over the frequency range 10<sup>1</sup>–10<sup>5</sup> are represented in **Figure 4a,b**. In accordance with what has been observed on planar electrodes, the mean impedance of PtSi NWs decreases

proportionally with the coating thickness. The phase angle of bare NWs exhibits a high variability between 10<sup>1</sup> and 10<sup>2</sup>, which, corresponds to noise induced by the potentiostat. The phase angle is close to –90° across the frequency range 10<sup>2</sup>–10<sup>5</sup> Hz, which indicates a highly capacitive behavior. When coated, the phase angle changes correspondingly with the coating thickness, which demonstrates an increase in the effective area and a shift to an ohmic-like behavior. Analogous trends have already been

obtained on PEDOT-coated microthreads,<sup>[60]</sup> PEDOT-coated 3D-structured microelectrodes,<sup>[10]</sup> and PEDOT nanotubes-covered electrodes.<sup>[61]</sup> The thermal noise can be extracted from these impedance measurements, for PtSi- and PEDOT:PSS-coated electrodes (layer thickness 400 nm) following the method described in Section S3 (Supporting Information). The thermal noise is found to be slightly lower with PEDOT: PSS coated electrodes ( $4.10 \mu\text{V} \pm 0.10 \mu\text{V}$ ) than PtSi NWs-based electrodes ( $4.37 \mu\text{V} \pm 0.29 \mu\text{V}$ ). Impedance values at 1 kHz have been extracted, and the data have been fitted using a linear function, as represented in Figure 4c. The impedance of bare PtSi NWs is 0.9 MOhm, and, as expected, the impedance value decreases when coated. Fitted trends indicate that thick coatings (700 nm) can extensively reduce the impedance by 18 times, from 0.9 MOhm for PtSi NWs to under 0.05 MOhm. However, thick coatings are less desirable for neuronal interfacing, as they affect the aspect ratio of the probes and may result in lower cell engulfment. Therefore, thinner coatings (<300 nm) are more relevant, already reducing the impedance at 1 kHz by three times to 0.3 MOhm. Similar trends have been observed on coated gold 3D-microelectrodes,<sup>[10]</sup> yet Jones et al. reported a maximal impedance decrease of only six times. The thinnest layer we obtained (40 nm) can also reduce the impedance at 1 kHz by almost half its value, from 0.9 to 0.5 MOhm. This is an excellent and promising result for applications in need of remarkably thin layers of PEDOT:PSS.

## 2.5. Equivalent Circuit Model

To further interpret these results, we conducted a theoretical analysis of the equivalent circuit model corresponding to our system, as shown in Figure 4d. Here, we demonstrate that our data can be fairly well described and modeled using a simple five-elements circuit, composed of an electrolyte resistance ( $R_s$ ), a charge-transfer resistance ( $R_{ct}$ ), a double layer capacitance ( $C_{dl}$ ), as well as a system capacitance ( $C_p$ ) and system resistance ( $R_p$ )<sup>[54]</sup> (see Section S4, Supporting Information, for the resulting equation). The electrolyte resistance,  $R_s$ , is measured between the working electrode and the platinum reference electrode; hence, it also includes all resistances originating from the access lines and contact pads.<sup>[33,62]</sup>  $R_{ct}$  and  $C_{dl}$  are both associated with phenomenon at the electrode/electrolyte interface.  $R_{ct}$  reflects the ability of the electrode–electrolyte interface circuit to resist the flow of charges from the ionic solution to the electronic conductor while  $C_{dl}$  accounts for the stored charge in the double-layer region, at the electrode–electrolyte junction.  $R_p$ , as well as  $C_p$ , are associated with the entire setup, comprising the initial contribution of the NEA regarding resistive and capacitive effects, as well as the measurement equipment, that is, connecting wires and a potentiostat. All  $|Z|$  data are accurately fitted ( $r^2 > 0.99$ ), over the frequency range  $10^2$ – $3 \cdot 10^5$  Hz, to avoid the impact of noise and artefacts caused by the potentiostat to the fitting algorithm, and examples of fitted data for bare PtSi and PEDOT:PSS coated NWs (410 nm layer) are displayed in (Figure 4e,f). Results indicated that  $R_p$  is very high (>50MOhm), and its effect is mainly prominent over low frequencies (< $10^2$ Hz), where background noise also affects the signal; hence, we chose to disregard this parameter in our calculations.

Parameter values with respect to the coating thickness are plotted in Figure 4g,h. The trends in Figure 4g show that  $C_p$  remains constant (average value  $100 \pm 9.5$  pF), and is lower than  $C_{dl}$ , which confirms that it represents the contribution of the set-up. Results demonstrate that  $C_{dl}$  is significantly greater than  $C_p$ , and  $C_p$  only affects the current flow starting around frequencies of 30 kHz. Therefore, system capacitances should not disturb neuronal recordings as events happen at lower frequencies. A sharp, thickness-dependent increase of  $C_{dl}$  value can be observed when the electrodes are coated, in comparison with bare PtSi (variation up to 11 764% measured between the PtSi and 620 nm-thick PEDOT:PSS layer). This demonstrates an important increase in the effective area when coated, as the capacitance value is directly proportional to the surface, as well as reflects the charge storage properties of PEDOT:PSS. Indeed, a higher capacitance value implies that more charge can be stored at the interface. On the other hand, Figure 4h indicates a decrease in  $R_{ct}$ , proportionally to the coating thickness, (96.5% decrease measured between the PtSi and 620 nm-thick PEDOT:PSS layer). This illustrates that the addition of PEDOT:PSS onto the probes promotes ionic to electronic charge transfers between the electrode and electrolyte, as well as confirms the increase in effective area as  $R_{ct}$  is inversely proportional to the surface. Hence, this study highlighted that the improvement in performance is induced by a combined effect of the PEDOT:PSS intrinsic properties and the increase in effective area, in particular the potential inherent porosity of the PEDOT:PSS layer.<sup>[57]</sup> Finally,  $R_s$  remains constant (average value  $536 \pm 48 \Omega$ ) and is lower than  $R_{ct}$ , in accordance with the fact that  $R_s$  represents the electrolyte resistance. The slight variations could be linked to the working electrode/counter electrode distance, as the placement of both is manual.

As a conclusion, we demonstrated that the circuit components match the physical characteristics of the system and can therefore be used as a baseline for further design optimization of the device and result interpretation.

## 2.6. Stimulation Performances of Nanowires-Based Probes

CV measurements were conducted to assess the charge storage capacity of the electrodes, using the conventional three-electrodes setup mentioned above. **Figure 5a** illustrates the cyclic voltammogram of uncoated PtSi NWs, within the  $-0.9$  and  $1.2$  V potential range, at a scan rate of  $200 \text{ mV s}^{-1}$  in a 0.9%w NaCl solution. The water electrolysis window ( $-0.9/1.1$  V) remains unchanged compared to planar configurations and is similar to the nanostructured Pt water window when cycled in PBS.<sup>[63]</sup> Coated NWs were characterized between  $-0.5$  and  $0.6$  V at  $200 \text{ mV s}^{-1}$  to avoid any undesirable faradaic reactions, as seen in Figure 5b. As expected, the presence of a coating increases the electroactive area and improves the charge storage properties, as confirmed in Figure 5c. Additionally, the coated NWs CV in Figure 5b indicate a high reversibility in the doping process, which implies beneficial properties with regard to ionic to electronic charge transfer at the electrode–electrolyte interface.<sup>[43]</sup> The cathodic CSC of the NWs-based electrodes has been calculated for different thicknesses, and the data have been fitted using linear functions, as represented in Figure 5c. As predicted, the CSC of the PEDOT:PSS coated electrodes is thickness-dependent. Fitted trends reveal

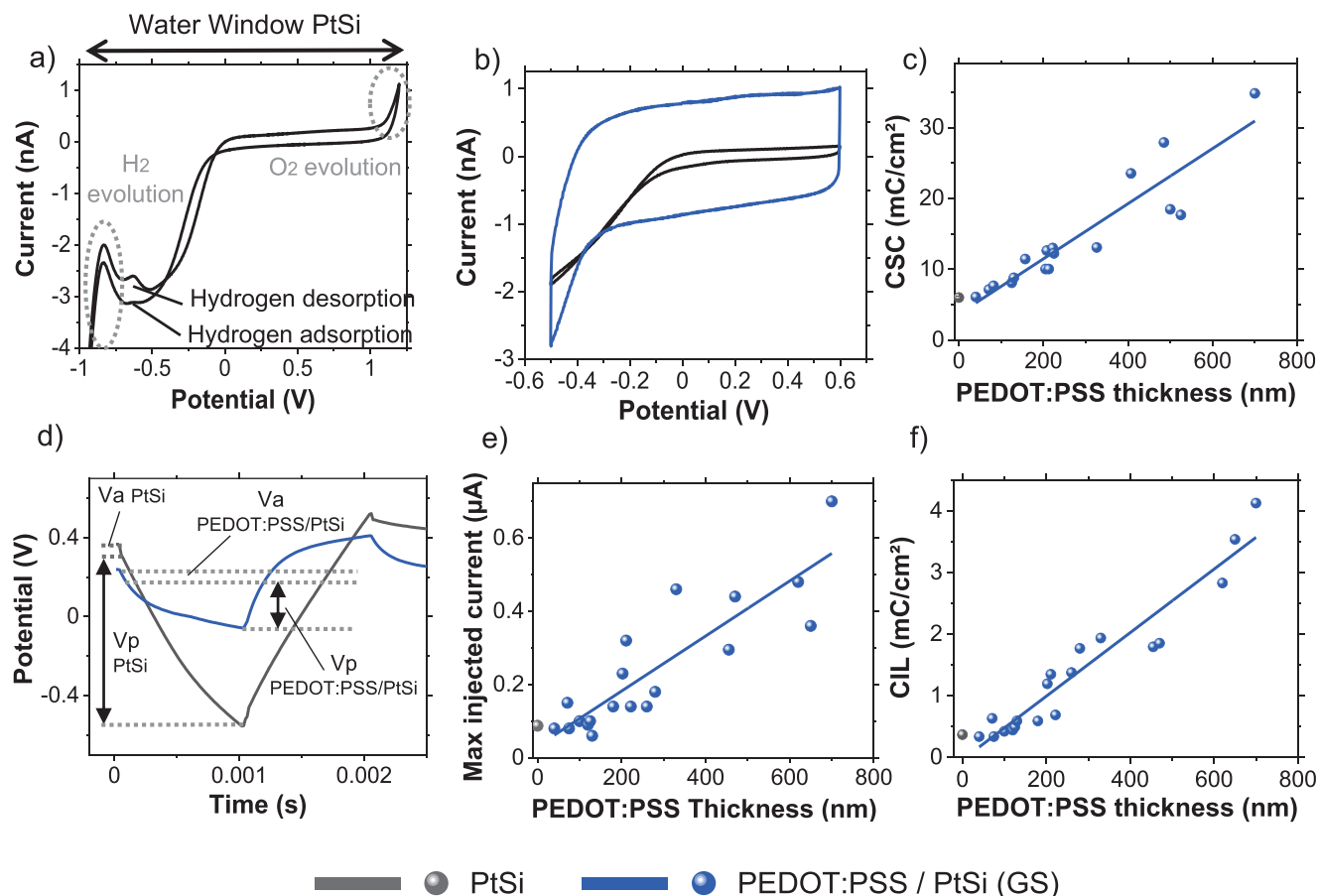


**Figure 5.** Complete electrochemical characterization of NWs-based electrodes regarding the stimulation performances. a) Cyclic voltammogram of PtSi NWs. b) Cyclic voltammograms of NWs before and after coating. The coating thickness here is 500 nm. c) Charge Storage Capacity values of bare and coated NWs as a function of coating thickness. d) Voltage transient comparison between PtSi and coated NWs (300 nm) at 0.08  $\mu\text{A}$  injection.  $V_a$  and  $V_p$  represent the access potential and the polarization potential, respectively. e) Current injection limit as a function of coating thickness. f) Charge Injection Limit as a function of coating thickness.

that thick coatings exhibit a CSC up to six times higher than bare electrodes, from 6 to 30  $\text{mC cm}^{-2}$  for bare and 700 nm coatings, respectively. 300 nm coatings double the CSC to 15  $\text{mC cm}^{-2}$  while (<100 nm) do not significantly improve the CSC.

The alteration of the PEDOT coating on the underlying PtSi nanowires was assessed via prolonged redox CV scanning within the  $-0.5$  to  $0.6$  V potential range, at a scan rate of  $200 \text{ mV s}^{-1}$  in a 0.9%w NaCl solution. In Section S5, Figure S4 (Supporting Information) shows the evolution of the CV scans and the corresponding CSCs values during the time of redox charge sweeping over 3000 redox cycles. For comparison, the CSCs of bare PtSi controls are provided. For PEDOT-coated nanowires, a slight increase in CSC during the redox cycling can be seen, which is associated with the initial reorganization of the polymer upon CV sweeping.<sup>[64,65]</sup> The corresponding CSC value stays constant along the redox cycles window. In addition, SEM images of PEDOT-coated nanowires and bare PtSi controls after the redox CV stimulations, suggested that all nanoelectrodes exhibited no physical delamination or degradation even after thousands of redox cycles, confirming excellent structural control and longevity. Robustness over prolonged CV redox scanning demonstrates excellent polymer stability under CV stimulation conditions and

suggests longer survival of the nanoelectrodes for recording applications.

To assess the NWs behavior during neuronal electrical stimulation, we performed voltage transient experiments. Bare and coated NWs were exposed to multiple cathodal-first, biphasic current pulses of a millisecond, with an interphase gap of 10  $\mu\text{s}$ , and an interpulse delay of 95 ms. An example of voltage transient response is represented in Figure 5d. Interestingly, NW-based electrodes exhibit a very small access potential, which is a common behavior in metallic microelectrodes.<sup>[32,52]</sup> Results show that, for a same injected current of 0.08  $\mu\text{A}$ , PtSi NWs present a higher  $V_p$  than PEDOT:PSS/PtSi NWs. This implies that coated probes reach their limit at higher currents; therefore, the CIL should be higher. This result is confirmed in Figure 5e,f. Indeed, the current injection limit and correspondent charge injection limit are greater for PEDOT:PSS coated NWs. Bare PtSi NWs present a CIL of 0.34  $\text{mC cm}^{-2}$ . In accordance with what has been observed on the CSC graph, 300 nm coatings already increase the CIL by 4 $\times$  (from 0.34  $\text{mC cm}^{-2}$  for PtSi NWs to 1.4  $\text{mC cm}^{-2}$ ), and the CIL is increased up to 10 $\times$ , to 3.53  $\text{mC cm}^{-2}$  at 700 nm. PEDOT:PSS coatings therefore improve both the recording and stimulation performances of PtSi 3D-nanoelectrodes. As anticipated, thicker

coatings enhance the properties more in comparison with ultra-thin coatings; however, the morphology of the layer can possibly interfere with cell engulfment for layers >300 nm.

To further position these results among other research groups developments, we compared the electrochemical performances of both our PEDOT:PSS coated planar MEA and nanowires configurations, with comparable neuronal interfacing configurations reported in the literature (see Table 1). Among the three categories, it is only the 3D nanostructures (third category) that significantly enhance cell engulfment on the electrodes, which is crucial for achieving high-resolution signal recording. We consider configurations to be comparable to ours when homogeneous layers of conductive coatings are deposited on metallic electrodes, indicating possible compatibility with an integration on nanostructures. We compared the results for Ø20 µm GS-coated electrodes and 300nm-coated NWs, the latter allowing us to keep the high aspect ratio of the electrodes. In both cases, we obtained specific impedance values at the state-of-the-art, with 6.36 MΩ µm<sup>-2</sup> for planar electrodes and 7.14 MΩ µm<sup>-2</sup> for NWs. Regarding the CIL values, planar electrodes also exhibit state-of-the-art performances with 6 mC cm<sup>-2</sup> while NWs possess a CIL of 1.4 mC cm<sup>-2</sup>. The exact contribution of the 3D-configuration in the CIL value decrease when compared to planar configuration remains under investigation. Nonetheless, the CIL value for NWs is within the range of reported values (from 0.9 to 6.2 mC cm<sup>-2</sup>) for a noticeably small surface area.

### 3. Conclusion

PtSi planar microelectrodes and NWs were successfully coated in PEDOT:PSS using electrodeposition. Various simple and reproducible polymerization routes have been investigated, from galvanostatic to potentiodynamic, showing a large range of layer morphology and performances. Electrochemical properties of bare and coated microelectrodes were assessed with EIS measurements, CV analysis, and voltage transient experiment, showing improvement for all diameters, notably for small diameters (down to 5 µm), where the state-of-the-art performance could envision the use of miniaturized MEA for studying the neuronal activity with much higher spatial resolution. Optimal deposition conditions were applied to 3D nanostructured electrodes based on NWs, resulting in conformal and homogeneous layers of PEDOT:PSS with thicknesses ranging from 700 to 40 nm, demonstrating the feasibility of selectively integrating ultra-thin layers of conducting polymer onto 3D-nano objects. Hence, the optimal cell engulfment should be maintained, as the aspect ratio of the NWs is kept for thicknesses of 300 nm and under. Electrochemical properties analysis showed that the presence of a conductive polymer coating leads to remarkable thickness-dependent characteristics combining low impedance, high charge storage capacity, and high charge injection limit. Ultra-thin layers of PEDOT:PSS, of thicknesses 100 nm and under, effectively maintain the nanometric dimensions of the structure, minimizing intrusiveness and perturbation of the sensing structure toward the cell. Moreover, it enhances the surface performance by reducing impedance by 50% at 1 kHz and provides a reduced mechanical mismatch at the electrode/cell interface due to the soft nature of the PEDOT:PSS material. Layers that are several hundreds of nanometers thick, with an optimal thickness of 300 nm

for the PEDOT:PSS layer, exhibit an impedance at 1 kHz that is three times lower than that of bare electrodes. Additionally, they demonstrate a CSC that is twice as high and CIL that is four times higher. Furthermore, these layers ensure the impeccable alignment of cells on the nanostructures, which promotes optimal electrode/cell interactions.

By combining, for the first time, nanometric high aspect ratio geometry with a high performance coated surface, PEDOT-coated 3D-nanostructured devices open new perspectives for neuronal interfacing, as they should enable the stimulation and recording of neuronal activity with acute spatial and signal resolution, while not impeding optimal cell engulfment.

### 4. Experimental Section

**NEAs Fabrication:** The 3D-nanostructured electrodes presented in this paper were fabricated using a CMOS-compatible process, similar to previously published.<sup>[17]</sup> A summary is included here for completeness (see Figure S5 in Section S6, Supporting Information). First, the nanowires were patterned on a 4" silicon-on-insulator wafer using a large-scale and cost-effective top-down approach through photolithography (i-line stepper) and anisotropic plasma reactive ionic etching steps. The aspect ratio of the probes could be tuned by adjusting the etch duration and performing sacrificial oxidation. Then, following the same protocol, the electrode base and conducting lines were structured down to the oxide layer. It is important to note that this structuration step was the first step of the process when fabricating planar microelectrodes. Next, a conformal platinum (Pt) layer was deposited on the wafer by Physical Vapor Deposition, followed by annealing to create a stable platinum silicide (PtSi) layer of ≈90 nm, forming a core-shell type nanostructure. The unreacted Pt layer was then removed using a selective chemical etching process. Next, the wafer was covered in conformal oxide layers to ensure the insulation of the electrode structures from any liquid environment. Last, the upper part of the probes was opened, creating vertical and conductive nanostructures. Finally, the chip was integrated onto a printed circuit board using the flip-chip method, resulting in a conventional MEA-like device with external contacts. Additionally, a glass cylinder was introduced for conducting electrochemical experiments or cell cultures.

**Electrochemical Characterization:** All electrochemical characterization and depositions were performed with a VMP3 Multichannel Potentiostat (Biologic Sciences Instruments). Cyclic voltammetry measurements were conducted with a Platinum counter electrode and a commercial Ag/AgCl reference electrode (LF-1.6-48, Innovative Instruments, Inc.) in 0.9%w NaCl solution. Impedance spectra were acquired from 1 Hz to 100 kHz with an amplitude of 20 mV, using a platinum counter electrode in 0.9%w NaCl solution (Sodium Chloride 99%, Sigma-Aldrich). PEDOT:PSS depositions were achieved using the same three-electrode setup, in a 10 mM 3,4-Ethylenedioxythiophene (EDOT) (Sigma-Aldrich), 10 mM Sodium poly(4styrenesulfonate) (Na:PSS) (Mw 70 000, Sigma-Aldrich) in deionized water prepared from a Millipore Milli-Q A10 system (18.2 MW cm<sup>-1</sup> resistivity). Voltage transient experiments were done using the conventional three electrode configuration, in a SP-240 potentiostat (Biologic Sciences Instruments) in Dulbecco's phosphate buffer saline solution.

**Morphological Characterization:** Focused-ion beam (FIB) milling and scanning electron microscopy (SEM) were performed with a Helios NanoLab 600i Dual Beam (FEI). AFM scans were performed using Dimension ICON (BRUCKER), and profilometer analysis was conducted on a Tencor P16+ (KLA TENCOR).

### Supporting Information

Supporting Information is available from the Wiley Online Library or from the author.

## Acknowledgements

This work was supported by the by the European Commission through the NEUREKA project (grant agreement number 863245) and by the LAAS-CNRS micro and nanotechnologies platform, a member of the Renatech French national network. The authors would like to thank Dr. Aurélie Lecestre and Adrian Laborde for their help during the fabrication process, Samuel Charlot for his assistance with the packaging of the NEAs, Dr. Venkata Suresh Reddy Vajrala for his guidance during electrochemical characterizations and Matthieu Sagot for his experience in data analysis.

## Conflict of Interest

The authors declare no conflict of interest.

## Data Availability Statement

The data that support the findings of this study are available from the corresponding author upon reasonable request.

## Keywords

charge injection limit, charge storage capacity, electrochemistry, electrophysiology, impedance, interfaces, nanoelectrodes, nanowires, PE-DOT:PSS

Received: March 16, 2023  
Revised: May 18, 2023  
Published online: July 23, 2023

- [1] M. Carter, J. Shieh, in *Guide to Research Techniques in Neuroscience*, Elsevier, Amsterdam, Netherlands **2015**, pp. 89–115.
- [2] G. N. Angotzi, F. Boi, A. Lecomte, E. Miele, M. Malerba, S. Zucca, A. Casile, L. Berdondini, *Biosens. Bioelectron.* **2019**, *126*, 355.
- [3] Y. Shi, R. Liu, L. He, H. Feng, Y. Li, Z. Li, *Smart Mater. Med.* **2020**, *1*, 131.
- [4] D. J. Bakkum, U. Frey, M. Radivojevic, T. L. Russell, J. Müller, M. Fiscella, H. Takahashi, A. Hierlemann, *Nat. Commun.* **2013**, *4*, 2181.
- [5] S. P. Lacour, S. Benmerah, E. Tarte, J. Fitzgerald, J. Serra, S. McMahon, J. Fawcett, O. Graudejus, Z. Yu, B. Morrison, *Med. Biol. Eng. Comput.* **2010**, *48*, 945.
- [6] M. E. J. Obien, K. Deligkaris, T. Bullmann, D. J. Bakkum, U. Frey, *Front. Neurosci.* **2015**, *8*, 00423.
- [7] K. A. Ludwig, N. B. Langhals, M. D. Joseph, S. M. Richardson-Burns, J. L. Hendricks, D. R. Kipke, *J. Neural Eng.* **2011**, *8*, 014001.
- [8] P. Fattahi, G. Yang, G. Kim, M. R. Abidian, *Adv. Mater.* **2014**, *26*, 1846.
- [9] D. R. Merrill, M. Bikson, J. G. R. Jefferys, *J. Neurosci. Methods* **2005**, *141*, 171.
- [10] P. D. Jones, A. Moskalyuk, C. Barthold, K. Gutöhrlein, G. Heusel, B. Schröppel, R. Samba, M. Giugliano, *Front. Neurosci.* **2020**, *14*, 405.
- [11] F. Santoro, J. Schnitker, G. Panaitov, A. Offenhäusser, *Nano Lett.* **2013**, *13*, 5379.
- [12] A. Fendyur, N. Mazurski, J. Shappir, M. E. Spira, *Front. Neuroengineering* **2011**, *4*.
- [13] Y. Kotani, H. Sawahata, S. Yamagiwa, R. Numano, K. Koida, T. Kawano, 2019 20th Intl. Conf. on Solid-State Sensors, Actuators and Microsystems & Eurosenors XXXIII (TRANSDUCERS & EUROSENSORS XXXIII), IEEE, Berlin, Germany **2019**, pp. 2205..
- [14] D. Decker, R. Hempelmann, H. Natter, M. Pirrung, H. Rabe, K. H. Schäfer, M. Saumer, *Adv. Mater. Technol.* **2019**, *4*, 1800436.
- [15] Z. C. Lin, C. Xie, Y. Osakada, Y. Cui, B. Cui, *Nat. Commun.* **2014**, *5*, 3206.
- [16] P. Shokooimehr, B. Cepkenovic, F. Milos, J. Bednár, H. Hassani, V. Maybeck, A. Offenhäusser, *Small* **2022**, *18*, 2200053.
- [17] A. Casanova, L. Bettamin, M.-C. Blatche, F. Mathieu, H. Martin, D. Gonzalez-Dunia, L. Nicu, G. Larrieu, *J. Phys. Condens. Matter* **2018**, *30*, 464001.
- [18] J. T. Robinson, M. Jorgolli, A. K. Shalek, M.-H. Yoon, R. S. Gertner, H. Park, *Nat. Nanotechnol.* **2012**, *7*, 180.
- [19] C. Xie, Z. Lin, L. Hanson, Y. Cui, B. Cui, *Nat. Nanotechnol.* **2012**, *7*, 185.
- [20] J. Kwon, S. Ko, J. Lee, J. Na, J. Sung, H.-J. Lee, S. Lee, S. Chung, H.-J. Choi, *Nanoscale* **2020**, *12*, 4709.
- [21] M. Dipalo, H. Amin, L. Lovato, F. Moia, V. Caprettini, G. C. Messina, F. Tantussi, L. Berdondini, F. De Angelis, *Nano Lett.* **2017**, *17*, 3932.
- [22] R. Liu, R. Chen, A. T. Elthakeb, S. H. Lee, S. Hinckley, M. L. Khraiche, J. Scott, D. Pre, Y. Hwang, A. Tanaka, Y. G. Ro, A. K. Matsushita, X. Dai, C. Soci, S. Biesmans, A. James, J. Nogan, K. L. Jungjohann, D. V. Pete, D. B. Webb, Y. Zou, A. G. Bang, S. A. Dayeh, *Nano Lett.* **2017**, *17*, 2757.
- [23] F. Santoro, S. Dasgupta, J. Schnitker, T. Auth, E. Neumann, G. Panaitov, G. Gompfer, A. Offenhäusser, *ACS Nano* **2014**, *8*, 6713.
- [24] J. Abbott, T. Ye, L. Qin, M. Jorgolli, R. S. Gertner, D. Ham, H. Park, *Nat. Nanotechnol.* **2017**, *12*, 460.
- [25] M. Ganji, A. C. Paulk, J. C. Yang, N. W. Vahidi, S. H. Lee, R. Liu, L. Hossain, E. M. Arneodo, M. Thunemann, M. Shigyo, A. Tanaka, S. B. Ryu, S. W. Lee, Y. Tchoe, M. Marsala, A. Devor, D. R. Cleary, J. R. Martin, H. Oh, V. Gilja, T. Q. Gentner, S. I. Fried, E. Halgren, S. S. Cash, S. A. Dayeh, *Nano Lett.* **2019**, *19*, 6244.
- [26] U. A. Aregueta-Robles, Y. L. Enke, P. M. Carter, R. A. Green, L. A. Poole-Warren, *IEEE Trans. Biomed. Eng.* **2020**, *67*, 3510.
- [27] J. Abbott, T. Ye, K. Krenek, R. S. Gertner, S. Ban, Y. Kim, L. Qin, W. Wu, H. Park, D. Ham, *Nat. Biomed. Eng.* **2020**, *4*, 232.
- [28] C. Chen, S. Ruan, X. Bai, C. Lin, C. Xie, I.-S. Lee, *Mater. Sci. Eng. C* **2019**, *103*, 109865.
- [29] J. D. Weiland, D. J. Anderson, M. S. Humayun, *IEEE Trans. Biomed. Eng.* **2002**, *49*, 1574.
- [30] W. Franks, I. Schenker, P. Schmutz, A. Hierlemann, *IEEE Trans. Biomed. Eng.* **2005**, *52*, 1295.
- [31] M. Mahmud, R. Pulizzi, E. Vasilaki, M. Giugliano, *Front. Neuroinformatics* **2014**, *8*, <https://doi.org/10.3389/fninf.2014.00026>.
- [32] Y. H. Kim, H. Koo, M. S. Kim, S.-D. Jung, *Sens. Actuators, B* **2018**, *273*, 718.
- [33] A. Wang, D. Jung, D. Lee, H. Wang, *ACS Appl. Electron. Mater.* **2021**, *3*, 5226.
- [34] V. S. Polikov, P. A. Tresco, W. M. Reichert, *J. Neurosci. Methods* **2005**, *148*, 1.
- [35] A. F. Renz, A. M. Reichmuth, F. Stauffer, G. Thompson-Steckel, J. Vörös, *J. Neural Eng.* **2018**, *15*, 061001.
- [36] S. F. Cogan, P. R. Troyk, J. Ehrlich, T. D. Plante, *IEEE Trans. Biomed. Eng.* **2005**, *52*, 1612.
- [37] S. Negi, R. Bhandari, L. Rieth, F. Solzbacher, *Biomed. Mater.* **2010**, *5*, 015007.
- [38] Q. Zeng, T. Wu, B. Sun, K. Xia, M. S. Humayun, 2018 IEEE Intl. Conf. on Cyborg and Bionic Systems (CBS), IEEE, Shenzhen, China **2018**, pp. 1–4.
- [39] N. Peixoto, K. Jackson, R. Samiyi, S. Minnikanti, 2009 Ann. Intl. Conf. of the IEEE Engineering in Medicine and Biology Society, IEEE, Minneapolis, MN, USA **2009**, pp.658–661.
- [40] A. Fujishiro, H. Kaneko, T. Kawashima, M. Ishida, T. Kawano, *Sci. Rep.* **2015**, *4*, 4868.
- [41] A. N. Dalrymple, M. Huynh, U. A. Robles, J. B. Marroquin, C. D. Lee, A. Petrossians, J. J. Whalen, D. Li, H. C. Parkington, J. S. Forsythe, R.

- A. Green, L. A. Poole-Warren, R. K. Shepherd, J. B. Fallon, *J. Neural Eng.* **2019**, *17*, 016015.
- [42] N. A. Batrisya Ismail, F. Abd-Wahab, W. W. Amani Wan Salim, 2018 IEEE-EMBS Conf. on Biomedical Engineering and Sciences (IECBES), IEEE, Sarawak, Malaysia **2018**, pp. 330–335.
- [43] V. Saunier, E. Flahaut, M.-C. Blatché, C. Bergaud, A. Maziz, *Biosens. Bioelectron.* **2020**, *165*, 112413.
- [44] H. B. Akkerman, P. W. M. Blom, D. M. De Leeuw, B. De Boer, *Nature* **2006**, *441*, 69.
- [45] V. Castagnola, C. Bayon, E. Descamps, C. Bergaud, *Synth. Met.* **2014**, *189*, 7.
- [46] M. Ganji, A. T. Elthakeb, A. Tanaka, V. Gilja, E. Hålgren, S. A. Dayeh, *Adv. Funct. Mater.* **2017**, *27*, 1703018.
- [47] L. Pigani, A. Heras, Á. Colina, R. Seeber, J. López-Palacios, *Electrochem. Commun.* **2004**, *6*, 1192.
- [48] E. Tamburri, S. Orlanducci, F. Toschi, M. L. Terranova, D. Passeri, *Synth. Met.* **2009**, *159*, 406.
- [49] H. Randriamahazaka, V. Noël, C. Chevrot, *J. Electroanal. Chem.* **1999**, *472*, 103.
- [50] A. K. Waafi, N. Gaio, W. F. Quiros-Solano, P. Dijkstra, P. M. Sarro, R. Dekker, *IEEE Sens. J.* **2020**, *20*, 1150.
- [51] D. R. Merrill, in *Somatosensory Feedback for Neuroprosthetics* (Ed.: B. Güçlü), Academic Press, Cambridge, MA, USA **2021**, pp. 77–150.
- [52] M. Ganji, A. Tanaka, V. Gilja, E. Hålgren, S. A. Dayeh, *Adv. Funct. Mater.* **2017**, *27*, 1703019.
- [53] C. Boehler, S. Carli, L. Fadiga, T. Stieglitz, M. Asplund, *Nat. Protoc.* **2020**, *15*, 3557.
- [54] H. S. Mandal, J. S. Kaste, D. G. Mchail, J. F. Rubinson, J. J. Pancrazio, T. C. Dumas, *Neuromodulation Technol. Neural Interface* **2015**, *18*, 657.
- [55] S. Eickhoff, J. C. Jarvis, *IEEE Trans. Biomed. Eng.* **2021**, *68*, 1658.
- [56] S. F. Cogan, *Ann. Rev. Biomed. Eng.* **2008**, *10*, 275.
- [57] Z. Aqrawe, B. Wright, N. Patel, Y. Vyas, J. Malmstrom, J. M. Montgomery, D. Williams, J. Travas-Sejdic, D. Svirskis, *Sens. Actuators, B* **2019**, *281*, 549.
- [58] A. Casanova, *Ph. D. Thesis*, Université de Toulouse, France **2016**.
- [59] Z. Aqrawe, J. Montgomery, J. Travas-Sejdic, D. Svirskis, *Sens. Actuators, B* **2018**, *257*, 753.
- [60] T. D. Y. Kozai, N. B. Langhals, P. R. Patel, X. Deng, H. Zhang, K. L. Smith, J. Lahann, N. A. Kotov, D. R. Kipke, *Nat. Mater.* **2012**, *11*, 1065.
- [61] H.-L. Chen, G.-Z. Tian, H. Yan, S.-X. Yang, D.-H. Kim, *Electrochim. Acta* **2021**, *404*, 139583.
- [62] X. F. Wei, W. M. Grill, *J. Neural Eng.* **2009**, *6*, 046008.
- [63] P. Daubinger, J. Kieninger, T. Unmüßig, G. A. Urban, *Phys. Chem. Chem. Phys.* **2014**, *16*, 8392.
- [64] X. Cui, D. C. Martin, *Sens. Actuators, B* **2003**, *89*, 92.
- [65] C. Boehler, F. Oberueber, S. Schlabach, T. Stieglitz, M. Asplund, *ACS Appl. Mater. Interfaces* **2017**, *9*, 189.
- [66] Y. Lu, T. Li, X. Zhao, M. Li, Y. Cao, H. Yang, Y. Y. Duan, *Biomaterials* **2010**, *31*, 5169.
- [67] S. Venkatraman, J. Hendricks, Z. A. King, A. J. Sereno, S. Richardson-Burns, D. Martin, J. M. Carmena, *IEEE Trans. Neural Syst. Rehabil. Eng.* **2011**, *19*, 307.
- [68] Y. H. Kim, G. H. Kim, M. S. Kim, S.-D. Jung, *Nano Lett.* **2016**, *16*, 7163.
- [69] S. Carli, M. Bianchi, E. Zucchini, M. Di Lauro, M. Prato, M. Murgia, L. Fadiga, F. Biscarini, *Adv. Healthcare Mater.* **2019**, *8*, 1900765.
- [70] S. Lee, T. Eom, M.-K. Kim, S.-G. Yang, B. S. Shim, *Electrochim. Acta* **2019**, *313*, 79.
- [71] R. Gerwig, K. Fuchsberger, B. Schroepel, G. S. Link, G. Heusel, U. Kraushaar, W. Schuhmann, A. Stett, M. Stelzle, *Front. Neuroengineering* **2012**, *5*, <https://doi.org/10.3389/fneng.2012.00008>.
- [72] Q. Li, K. Nan, P. Le Floch, Z. Lin, H. Sheng, T. S. Blum, J. Liu, *Nano Lett.* **2019**, *19*, 5781.
- [73] R. Liu, J. Lee, Y. Tchoe, D. Pre, A. M. Bourhis, A. D'antonio-Chronowska, G. Robin, S. H. Lee, Y. G. Ro, R. Vatsyayan, K. J. Tonsfeldt, L. A. Hossain, M. L. Phipps, J. Yoo, J. Nogan, J. S. Martinez, K. A. Frazer, A. G. Bang, S. A. Dayeh, *Adv. Funct. Mater.* **2022**, *32*, 2108378.